

Electron swarm parameters in C₂H₂, C₂H₄ and C₂H₆: measurements and kinetic calculations

N R Pinhão¹ , D Loffhagen² , M Vass^{3,4} , P Hartmann³ , I Korolov⁴ , S Dujko⁵ , D Bošnjaković⁵  and Z Donkó³ 

¹Instituto de Plasmas e Fusão Nuclear, Instituto Superior Técnico, Universidade de Lisboa, Av. Rovisco Pais, 1049-001 Lisboa, Portugal

²Leibniz Institute for Plasma Science and Technology, Felix-Hausdorff-Str. 2, D-17489 Greifswald, Germany

³Institute for Solid State Physics and Optics, Wigner Research Centre for Physics, 1121 Budapest, Konkoly Thege Miklós str. 29-33, Hungary

⁴Department of Electrical Engineering and Information Science, Ruhr-University Bochum, D-44780, Bochum, Germany

⁵Institute of Physics, University of Belgrade, Pregrevica 118, 11080 Belgrade, Serbia

E-mail: npinhao@ctn.tecnico.ulisboa.pt

Received 19 November 2019, revised 30 January 2020

Accepted for publication 19 February 2020

Published 31 March 2020



CrossMark

Abstract

This work presents swarm parameters of electrons (the bulk drift velocity, the bulk longitudinal component of the diffusion tensor, and the effective ionization frequency) in C₂H_{*n*}, with *n* = 2, 4, and 6, measured in a scanning drift tube apparatus under time-of-flight conditions over a wide range of the reduced electric field, 1 Td ≤ *E/N* ≤ 1790 Td (1 Td = 10⁻²¹ V m²). The effective steady-state Townsend ionization coefficient is also derived from the experimental data. A kinetic simulation of the experimental drift cell allows estimating the uncertainties introduced in the data acquisition procedure and provides a correction factor to each of the measured swarm parameters. These parameters are compared to results of previous experimental studies, as well as to results of various kinetic swarm calculations: solutions of the electron Boltzmann equation under different approximations (multiterm and density gradient expansions) and Monte Carlo simulations. The experimental data are consistent with most of the swarm parameters obtained in earlier studies. In the case of C₂H₂, the swarm calculations show that the thermally excited vibrational population should not be neglected, in particular, in the fitting of cross sections to swarm results.

Supplementary material for this article is available [online](#)

Keywords: electron swarm parameters, drift tube measurements, kinetic theory and computations

1. Introduction

Acetylene (C₂H₂), ethylene (C₂H₄) and ethane (C₂H₆) are relatively simple hydrocarbons useful in specialized applications such as plasma-assisted combustion [1–6], the fabrication of diamond-like films [7], graphene and carbon nanostructures [8], and particle detectors [9]. They are also involved in various chemical reactions in fusion plasmas [10], the Earth's atmosphere [11] and in planetary atmospheric chemistry [12].

Knowledge on both electron collision cross sections and electron swarm parameters is needed for the quantitative modeling of plasmas. However, with the exception of the drift velocity, which was measured e.g. in [13–17] for C₂H₂, in [13, 16–23] for C₂H₄, and in [13, 15–17, 19, 24, 25] for C₂H₆, further experimental transport and ionization coefficients have less frequently been reported for these hydrocarbon gases. Measurements of the longitudinal component of the diffusion tensor under time-of-flight (TOF) conditions were additionally reported in [14] for C₂H₂, [18–20] for

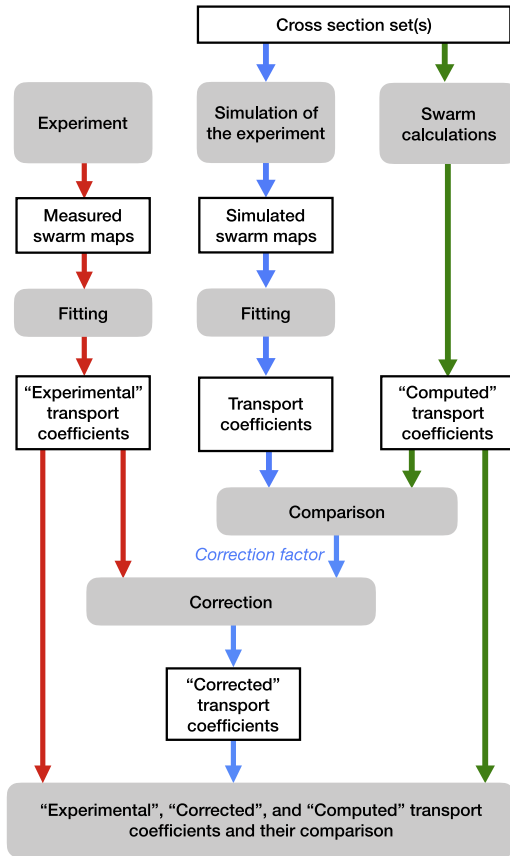


Figure 1. Graphical representation of the work reported in this article. The red arrows indicate the path from the measurements to the ‘Experimental’ transport coefficients and ionization frequencies via fitting of the measured ‘swarm maps’. Another ‘Corrected’ set of experimental data is also derived based on a correction procedure which is aided by simulations of the experimental setup and related data acquisition (indicated by blue arrows) and by kinetic computations of the swarm parameters. The results of these calculations (‘Computed’ transport coefficients) are also compared to the experimental data (green arrows).

C_2H_4 , and [19, 24] for C_2H_6 . Hasegawa and Date [13] also determined the effective ionization coefficient by the steady-state Townsend (SST) method for seven organic gases including acetylene, ethylene, and ethane. In addition to the drift velocity for C_2H_6 , Kersten [25] measured the effective ionization coefficient under TOF conditions for a narrow range of the reduced electric field, E/N . Furthermore, measured data for the effective SST ionization coefficient have been reported e.g. in [26] for C_2H_2 , in [26, 27] for C_2H_4 , and in [28–30] for C_2H_6 .

The aim of this work is (i) to determine the electron transport and ionization coefficients in C_2H_2 , C_2H_4 and C_2H_6 gases in a wide range of E/N , (ii) to compare these results with those obtained in earlier investigations of these gases, and (iii) to compare the experimental data with those obtained from kinetic calculations and simulations using up-to-date electron collision cross section sets.

The workflow of our studies can be followed with the aid of figure 1. The red arrows show the path to the ‘Experimental transport coefficients’ including the effective ionization frequencies. The first step along this path consists of the

measurements carried out with our scanning drift tube apparatus. This is a pulsed system, which is described in section 2. It records current traces generated by electrons collected from clouds that arrive after having flown over the drift region. The results of the experiments are the so-called ‘swarm maps’ which are collections of these current traces for a number of drift gap length values. The swarm parameters are derived from the measured swarm maps via a fitting procedure that assumes that the current measured in the experiment is proportional to the electron density. For the fitting we use the theoretical form of the electron density in the presence of an electric field pointing in the $-z$ direction and under TOF conditions:

$$n_e(z, t) = \frac{n_0}{(4\pi D_L t)^{1/2}} \exp \left[\nu_{\text{eff}} t - \frac{(z - Wt)^2}{4D_L t} \right]. \quad (1)$$

This is the solution of the spatially one-dimensional continuity equation and represents a Gaussian pulse drifting along the z direction with the bulk drift velocity, W , and diffuses along the center-of-mass according to the bulk longitudinal component of the diffusion tensor D_L . Here n_0 is the electron density at $z = 0$ at time $t = 0$, and ν_{eff} is the effective ionization frequency. From the fitting procedure we obtain W , D_L , and ν_{eff} . The application of the relation [31]

$$\frac{1}{\alpha_{\text{eff}}} = \frac{W}{2\nu_{\text{eff}}} + \sqrt{\left(\frac{W}{2\nu_{\text{eff}}} \right)^2 - \frac{D_L}{\nu_{\text{eff}}}} \quad (2)$$

allows us to derive the effective SST ionization coefficient, α_{eff} , as well.

The assumption that the measured current is proportional to the electron density is, in fact, an approximation, due to two reasons. First, the measured current is generated by moving charges in the detector of the system (see later). In our previous work [32] we have found that the detection sensitivity depends on the gas pressure and the collision cross sections, which both influence the free path of the electrons. This means that any variation of the energy distribution along the z direction in the electron cloud may result in a distortion of the detected pulse and a deviation from the analytical fitting function (1) assumed. Second, the measured current is proportional to the electron flux consisting of the advective and diffusive component. The advective component is proportional to the electron density, where the coefficient of proportionality is the flux drift velocity, and the diffusive component is proportional to the gradient of the electron density. Using Ramo’s theorem [33], it can be shown that for the experimental conditions considered in the present work, the contribution of the diffusive component to the current is negligible compared to the contribution of the advective component, except in the early stage of the swarm development when the spatial gradients of the electron density are more significant.

The errors introduced by the first effect mentioned above can be quantified by a procedure, which is marked by blue arrows in figure 1. We carry out a (Monte Carlo (MC)) simulation of the electrons’ motion in the experimental system. This simulation generates the *same* type of swarm maps,

which are obtained in the experiments, and a set of swarm parameters is derived via the *same* fitting procedure as in the case of experimental swarm maps. The transport coefficients and ionization frequencies obtained in this way are compared with the ‘Computed’ ones, originating from kinetic swarm calculations. We note that (i) this comparison does not include any experimental data, (ii) the system’s simulations use the *same* cross section set as in the kinetic swarm calculations, and (iii) uncertainties of the collision cross sections used have little influence on the outcome of the comparison of the parameter sets obtained by swarm calculations and simulations of the experimental system. The result of this comparison is gas- and E/N -dependent correction factors that are applied to the experimental data, providing sets of ‘Corrected’ experimental transport and ionization coefficients. Details are given below in section 4.

The two (raw and corrected) sets of experimental results are compared with swarm parameters derived from kinetic calculations based on solutions of the electron Boltzmann equation (BE) and on MC simulations as described in detail in section 3. The application of these different approaches allows us to mutually verify the accuracy of the different methods and test the assumptions used by each method. The ‘flow’ of this process is indicated by the green arrows in figure 1.

The manuscript is organized as follows: in section 2 we give a concise description of our experimental setup. A discussion of the various computational methods and the resulting swarm parameters is presented in section 3, and section 4 describes the correction procedure applied to the experimental data. It is followed by the discussion of the results in section 5. This section comprises the presentation of the present experimental results for each gas and their comparison with previously available measured data as well as the comparison between transport parameters and ionization coefficients computed using the various numerical methods and the present experimental data. Section 6 gives our concluding remarks.

2. Experimental system

The experiments are based on a ‘scanning’ drift tube apparatus, of which the details have been presented in [34]. This apparatus has already been applied for the measurements of transport and ionization coefficients of electrons in various gases: argon, synthetic air, methane, deuterium [35] and carbon dioxide [36]. In contrast to previously developed drift tubes, our system allows for recording of ‘swarm maps’ that show the spatio-temporal development of electron clouds under TOF conditions. The simplified scheme of our experimental apparatus is shown in figure 2.

The drift cell is situated within a vacuum chamber made of stainless steel. The chamber can be evacuated by a turbomolecular pump backed with a rotary pump to a level of about 1×10^{-7} mbar. The pressure of the working gases inside the chamber is measured by a Pfeiffer CMR 362 capacitive gauge.

Ultraviolet light pulses ($1.7 \mu\text{J}$, 5 ns) of a frequency-quadrupled diode-pumped YAG laser enter the chamber via a feedthrough with a quartz window and fall on the surface of a Mg disk used as photoemitter. This disk is placed at the center of a stainless steel electrode with 105 mm diameter that serves as the cathode of the drift cell. The detector that faces the cathode at a distance L_1 consists of a grounded nickel mesh (with $T = 88\%$ ‘geometric’ transmission and 45 lines/inch density) and a stainless steel collector electrode that is situated at a distance of $L_2 = 1$ mm behind the mesh.

Electrons emitted from the Mg disk fly towards the collector under the influence of an accelerating voltage that is applied to the cathode. This voltage is established by a BK Precision 9185B power supply. Its value is adjusted according to the required E/N for the given experiment and the actual value of the gap (L_1) during the scanning process, where E/N is ensured to be fixed. The current of the detector system is generated by the moving charges within the mesh-collector gap: according to the Shockley–Ramo theorem [33, 37, 38] the current induced by an electron moving in a gap between two plane-parallel electrodes with a velocity v_z perpendicular to the electrodes is $I = -e_0 v_z / L$, where $-e_0$ is the charge of the electron and L is the distance between the electrodes ($L = L_2$ in our case). Accordingly, in our setting the measured current at a given time t is

$$I(t) = c \sum_k v_{z,k}(t), \quad (3)$$

where c is a constant. The summation goes over all electrons being present in the volume bounded by the mesh and the collector at time t , and $v_{z,k}$ is the velocity component of the k th electron in z direction.

Electrons entering the detector region (the gap between the nickel mesh and the collector) contribute to the measured current until their first collisions with the gas molecules, as these collisions randomize the angular distribution of their velocities. Therefore, the free path of the electrons plays a central role in the magnitude of the current. For conditions when this free path is longer than the detector gap, the electron sticking property of the collector surface plays a crucial role too, as reflected electrons generate a current contribution with an opposite sign with respect to that generated by the ‘incoming’ electrons. According to the above effects, which have been explored to some details in [32], the sensitivity of the detector changes with the nature of the gas (magnitudes and energy dependence of the electron collision cross sections), the pressure, as well as the energy distribution of the electrons. This dependence is the primary reason which calls for a correction of the measured transport and ionization coefficients as discussed in more details in section 4.

The collector current is amplified by a high speed current amplifier (type Femto HCA-400M) connected to the collector, with a virtually grounded input, and is recorded by a digital oscilloscope (type Picoscope 6403B) with sub-ns time resolution. Data collection is triggered by a photodiode that senses the laser light pulses. The low light pulse energy necessitates averaging over typically 20 000–150 000 pulses. The

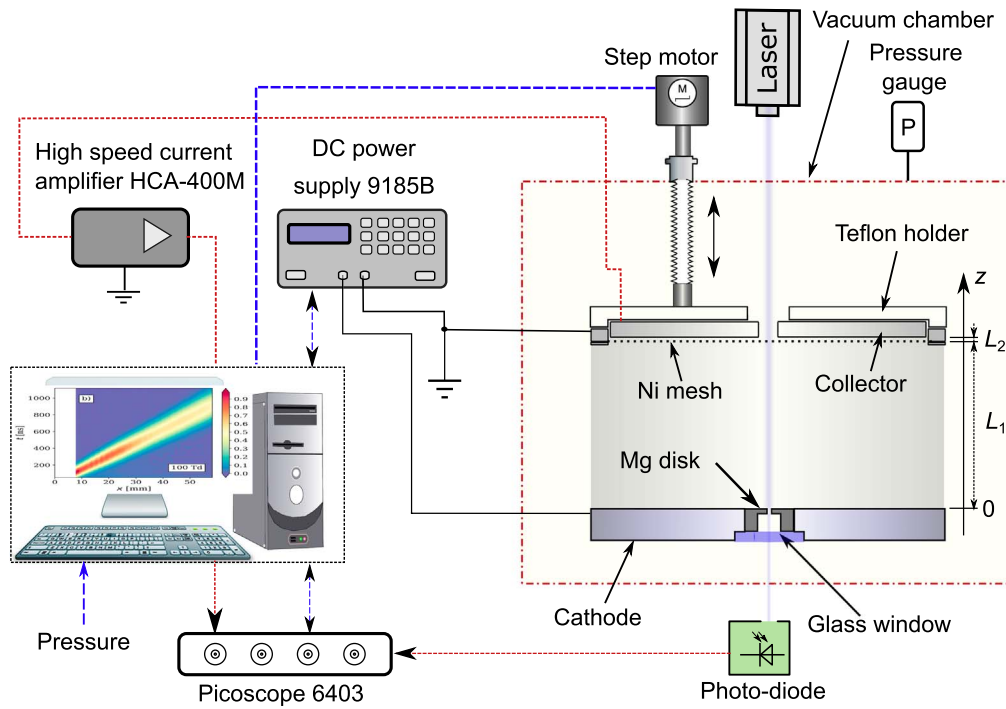


Figure 2. Simplified schematic of the scanning drift tube apparatus.

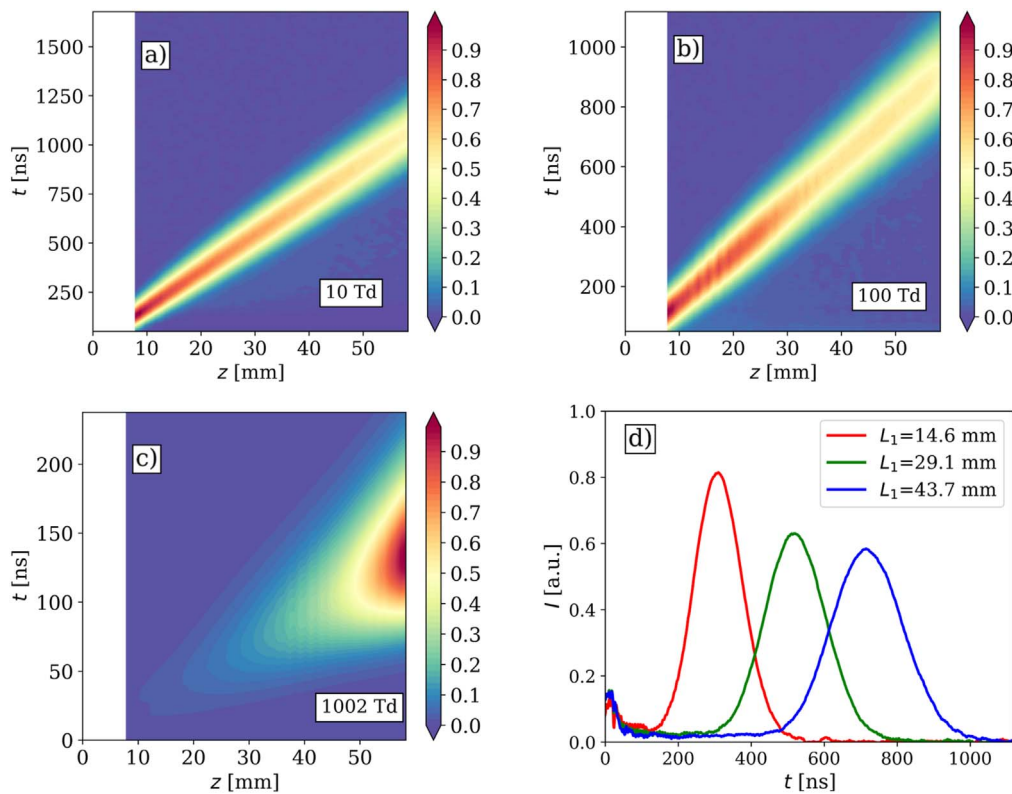


Figure 3. (a)–(c) Swarm maps recorded in C_2H_6 for different values of E/N , as indicated. (d) Vertical cuts of the swarm map of (b), which are the measured current traces at the drift length values given in the legend. The pulses have nearly Gaussian shapes. The ‘shift’ of the pulses with increasing drift length (L_1) is the manifestation of the drift, while their widening is due to (longitudinal) diffusion. As ionization in C_2H_6 is weak at $E/N = 100 \text{ Td}$, the amplitude of the pulses decreases with increasing L_1 due to the widening of the pulse.

experiment is fully controlled by a computer using LabView software.

During the course of the measurements current traces are recorded for several values of the gap length. The grid and the collector are moved together by a step motor connected to a micrometer screw mounted via a vacuum feedthrough to the vacuum chamber. The distance between the cathode and the mesh, i.e. the ‘drift length’, can be set within a range of $L_1 = (7.8\text{--}58.3)$ mm. Here, we use 53 positions within this domain.

Sequences of the measured current traces are subsequently merged to form ‘swarm maps’, which provide information about the spatio-temporal development of the electron cloud. Figures 3(a)–(c) illustrates such swarm maps, obtained in experiments on C_2H_6 , for different values of the reduced electric field. The qualitative behavior of the swarm is directly seen in these pictures: the slope of the region with appreciable current indicates the drift of the cloud, the widening of this region is related to (longitudinal) diffusion, while an increasing amplitude (as seen in panel (c)) is an indication of ionization. Figure 3(d) displays vertical ‘cuts’ of the map shown in panel (b), for $E/N = 100$ Td. These cuts are, actually, the current traces recorded in the measurements at different gap length values.

3. Simulation of the electron swarm

The experimental studies of the electron transport are supplemented by numerical modeling and simulation. In addition to MC simulations, three different methods are applied to solve the BE for electron swarms in a background gas with density N and acted upon by a constant electric field, \vec{E} : a multiterm method for the solution of the time-independent BE under spatially homogeneous and SST conditions, respectively, and the S_n method applied to a density gradient expansion of the electron velocity distribution function (EVDF). They differ in their initial physical assumptions and in the numerical algorithms used and provide different properties of the electron swarms

Details of the different BE methods, as well as main aspects of the MC simulation have been discussed in [36], and we just provide a brief discussion below.

In the following, the electric field is parallel to the z axis and points in the negative direction, $\vec{E} = -E\vec{e}_z$, and θ is the angle between \vec{v} and \vec{E} . Moreover, we assume that the spatial and time scales, respectively, exceed the energy relaxation length and time, such that the transport properties of the electrons do not change with time t and distance z any longer. That is, the electrons have reached a hydrodynamic regime characterizing a state of equilibrium of the system where the effects of collisions and forces are dominant and the EVDF, $f(\vec{r}, \vec{v}, t)$, has lost any memory of the initial state.

We base our studies on the electron collision cross section sets from Song *et al* [39] for acetylene, Fresnet *et al* [40] for ethylene and Shishikura *et al* [24] for ethane. The cross sections for acetylene and ethane were extended to

electron kinetic energies, ϵ , of 1000 eV by fitting a function with a $\log(\epsilon)/\epsilon$ dependence, according to the Born-Bethe high-energy approximation, to the tail of the original cross sections.

The C_2H_2 data set includes the momentum transfer cross section for elastic collisions, three vibrational cross sections for single quanta excitation of modes ν_1/ν_3 , ν_4/ν_5 and ν_2 (the first two unresolved) and one vibrational cross section for two quanta excitation of $\nu_4+\nu_5$, three electronic excitation cross sections, the total electron-impact ionization cross section and the total dissociative electron attachment cross section for C_2H_2 leading to the formation of C_2H^- , H^- and C_2^- , respectively.

The C_2H_4 data set includes the momentum transfer cross section, two lumped vibrational cross sections with thresholds at 0.118 and 0.365 eV, three electronic excitation cross sections, the total electron ionization cross section and a collision cross section for electron attachment.

Finally, the C_2H_6 set of collision cross sections includes the momentum transfer cross section, three lumped vibrational cross sections with thresholds at 0.112, 0.167 and 0.36 eV, two electronic excitation cross sections, the total electron ionization cross section and an electron attachment cross section.

All of the above cross section sets were developed neglecting the population of thermally excited vibrational states and superelastic processes. The implications of this approximation are discussed in section 5.4.

3.1. BE methods

3.1.1. Multiterm method for spatially homogeneous conditions. In this approach, to describe $f(\vec{r}, \vec{v}, t)$ (abbreviated by BE 0D in the figures shown in section 5), we consider that the EVDF is spatially homogeneous (0D) and the electron density changes exponentially in time according to $n_e(t) \propto \exp(\nu_{\text{eff}} t)$ at the scale of the swarm. Here, the effective ionization frequency $\nu_{\text{eff}} = \nu_i - \nu_a$ is the difference of the ionization (ν_i) and attachment (ν_a) frequencies. In this case we can neglect the dependence of f on the space coordinates and write the EVDF under hydrodynamic conditions as

$$f(\vec{v}, t) = \hat{F}(\vec{v})n_e(t). \quad (4)$$

The corresponding microscopic and macroscopic properties of the electrons are determined by the time-independent, spatially homogeneous BE for $\hat{F}(\vec{v})$. As this distribution is symmetric around the field direction, it can be expanded with respect to the angle θ in Legendre polynomials $P_n(\cos \theta)$ with $n \geq 0$. Substituting this expansion in the BE leads to a hierarchy of partial differential equations for the coefficients $\hat{f}_n(v)$ of this expansion. The resulting set of equations with typically eight expansion coefficients is solved employing a generalized version of the multiterm solution technique for weakly ionized steady-state plasmas [41] adapted to take into

account the ionizing and attaching electron collision processes.

Using the computed expansion coefficients $\hat{f}_n(v)$, we obtain the effective ionization frequency, ν_{eff} , and the flux drift velocity

$$w = -\mu E, \quad (5)$$

where μ is the flux mobility. Explicit formulas of these transport parameters obtained by the BE 0D method can be found in [36].

3.1.2. Multiterm method for SST conditions. This approach to describe the EVDF (abbreviated by BE SST in the figures shown in section 5) takes into account that $f(\vec{r}, \vec{v}, t)$ has reached SST conditions so that the mean transport properties of the electrons are time-independent, do not vary with position any longer, and the electron density assumes an exponential dependence on the distance according to $n_e(z) \propto \exp(\alpha_{\text{eff}} z)$. Thus, we can neglect the dependence of f on time and write the EVDF under SST conditions as

$$f(z, \vec{v}) = \tilde{F}^{(S)}(\vec{v}) n_e(z), \quad (6)$$

where the upper index (S) denotes SST conditions. In accordance with the procedure described in section 3.1.1, the corresponding microscopic and macroscopic properties of the electrons are determined by the steady-state, spatially homogeneous BE for $\tilde{F}^{(S)}(\vec{v})$. Since this distribution is again symmetric around the direction of the field, it can be expanded in Legendre polynomials $P_n(\cos \theta)$ with $n \geq 0$. The substitution of this expansion into the BE leads to a set of partial differential equations for the expansion coefficients $\tilde{f}_n^{(S)}(v)$, which is solved efficiently by a modified version of the multiterm method [41] adapted to treat SST conditions [36].

In this approach, the effective SST ionization coefficient is directly given by

$$\alpha_{\text{eff}} = \frac{\nu_{\text{eff}}^{(S)}}{v_m^{(S)}}. \quad (7)$$

Here, $\nu_{\text{eff}}^{(S)}$ and $v_m^{(S)}$ are the effective ionization frequency and mean velocity at SST conditions, respectively, which are calculated by means of the computed expansion coefficients $\tilde{f}_n^{(S)}(v)$ [36].

3.1.3. Density gradient representation. When ionization or attachment processes become important in TOF experiments, the electron swarm can no longer be considered homogeneous and the electron density gradients become significant.

This approach to describe the electron swarm at hydrodynamic conditions (labeled as BE DG below) is based on an expansion of the EVDF with respect to space gradients of the electron density n_e , of consecutive order. In this case, f depends on (\vec{r}, t) only via the density $n_e(\vec{r}, t)$ and can be written as an expansion on the gradient operator ∇ according

to

$$f(\vec{r}, \vec{v}, t) = \sum_{j=0} F^{(j)}(\vec{v}) \odot^j (-\nabla)^j n_e(\vec{r}, t), \quad (8)$$

where the expansion coefficients $F^{(j)}(\vec{v})$ are tensors of order j depending only on \vec{v} , and \odot^j indicates a j -fold scalar product [42]. Note that the first coefficient $F^{(0)}(\vec{v})$ corresponds to the function $\hat{F}(\vec{v})$ above, for spatially homogeneous conditions (see section 3.1.1).

The expansion coefficients $F^{(j)}$ of order j are obtained from a hierarchy of equations for each component, which all have the same structure and depend on the previous orders. In particular, to obtain the transport coefficients measured in TOF experiments, a total of five equations are required, namely for the expansion coefficients $F^{(0)}$, $F_z^{(1)}$, $F_T^{(1)}$, $F_{zz}^{(2)}$ and $F_{TT}^{(2)}$. In the present study, these equations are solved using a variant of the finite element method given in [43] in a $(v, \cos \theta)$ grid.

From the above expansion coefficients we obtain two sets of transport coefficients: the flux coefficients, neglecting the contribution of non-conservative processes and equivalent to those obtained by the BE 0D approach described in section 3.1.1, and the bulk coefficients including a contribution from ionization and attachment. The latter are, the bulk drift velocity

$$W = w + \int \tilde{\nu}_{\text{eff}}(v) F_z^{(1)}(\vec{v}) d\vec{v} \quad (9)$$

with $\tilde{\nu}_{\text{eff}}(v) = \nu N[\sigma^i(v) - \sigma^a(v)]$ where σ^i and σ^a are, respectively, the ionization and attachment cross sections; and the longitudinal and transverse components of the diffusion tensor

$$D_L = \int v_z F_z^{(1)}(\vec{v}) d\vec{v} + \int \tilde{\nu}_{\text{eff}}(v) F_{zz}^{(2)}(\vec{v}) d\vec{v}, \quad (10)$$

$$D_T = \frac{1}{2} \left\{ \int v_T F_T^{(1)}(\vec{v}) d\vec{v} + \int \tilde{\nu}_{\text{eff}}(v) F_{TT}^{(2)}(\vec{v}) d\vec{v} \right\}. \quad (11)$$

Note that the first terms of the right-hand side of equations (9)–(11) are the flux component. Further details can be found in [36].

The effective or apparent Townsend ionization coefficient α_{eff} , as determined in SST experiments, can be computed from the TOF parameters using equation (2).

3.2. MC technique

In the MC simulation technique, we trace the trajectories of the electrons in the external electric field and under the influence of collisions. As the degree of ionization under the swarm conditions considered here is low, only electron-background gas molecule collisions are taken into account. The motion of the electrons with mass m_e between collisions is described by their equation of motion

$$m_e \frac{d^2 \vec{r}}{dt^2} = -e_0 \vec{E}. \quad (12)$$

The electron trajectories between collisions are determined by integrating this equation numerically over time steps of

duration Δt ranging between 0.5 and 2.5 ps for the various conditions. While this procedure is totally deterministic, the collisions are handled in a stochastic manner. The probability of the occurrence of a collision is computed after each time step, for each of the electrons, as

$$P(\Delta t) = 1 - \exp[-N\nu\sigma^T(v)\Delta t]. \quad (13)$$

The occurrence of a collision is determined by comparing $P(\Delta t)$ with a random number with a uniform distribution over the (0, 1) interval. The type of collision is also selected in a random manner taking into account the values of the cross sections of all possible processes at the energy of the colliding electron. For a more detailed description see [36].

The transport parameters (labeled as MC below) are determined as

$$W = \frac{d}{dt} \left[\frac{\sum_{j=1}^{N_e(t)} z_j(t)}{N_e(t)} \right] \quad (14)$$

and

$$w = \frac{1}{N_e(t)} \sum_{j=1}^{N_e(t)} \frac{dz_j(t)}{dt}, \quad (15)$$

respectively, for the *bulk* and *flux* drift velocities, where $N_e(t)$ is the number of electrons in the swarm at time t . The bulk longitudinal and transverse components of the diffusion tensor are

$$D_L = \frac{1}{2} \frac{d}{dt} [\langle z^2(t) \rangle - \langle z(t) \rangle^2], \quad (16)$$

$$D_T = \frac{1}{4} \frac{d}{dt} [\langle x^2(t) + y^2(t) \rangle], \quad (17)$$

and the effective ionization frequency is given by

$$\nu_{\text{eff}} = \frac{d \ln(N_e(t))}{dt}. \quad (18)$$

Furthermore, the effective SST ionization coefficient α_{eff} is also calculated according to relation (2) using (14), (16) and (18).

All results of calculated electron swarm parameters presented in this work were additionally verified by independent MC simulations and calculations based on multi-term solutions of the electron BE developed by the Belgrade group [44, 45]. For clarity, these results are not included in the figures shown in the next sections, but are available from the authors on request.

As it was already mentioned in the Introduction and is discussed in somewhat more detail in the next section, MC simulations are also applied in the simulation of the electrons' motion in the experimental system, assisting a correction procedure of the experimental data.

4. Correction of the experimental results

To quantify the effect caused by the variations of the electron energy distribution along the swarm, that in turn makes the detection sensitivity time-dependent, MC simulations of the

experimental system have been carried out for most of the sets of conditions (p , E/N) in the experiments. These simulations generate swarm maps, similarly to those measured, and a set of swarm parameters is derived from these maps via exactly the same fitting procedure as in the case of the experimental data. The transport parameters and ionization frequencies obtained from the simulations of the setup are compared with those obtained from kinetic swarm calculations based on the solution of the electron BE, where the same electron collision cross section sets are used. Good agreement between the two sets of swarm parameters implies that the assumption made in the fitting of the experimental data, i.e. the use of the theoretical form (1) of $n_e(z, t)$ as a fit to the measured data, is acceptable. In contrast, strong deviations indicate that this assumption is not applicable for the given condition. We note that no experimental data are involved in this procedure.

In these MC simulations the electrons leaving the cathode had an initial energy of 1 eV, which is a realistic value considering the photon energy and the work function of the cathode material. These electrons were started with a uniform angular distribution over the positive half sphere. The sensitivity of the computed swarm maps on this latter assumption is not expected to be strong because the collisions quickly randomize the initial directions of the electrons. As in these simulations the motion of the electrons in the whole experimental system is described, the dependence of the detector's sensitivity on the energy of the electrons entering the mesh-collector gap is 'automatically' included as the detector current generated by these electrons is computed directly.

Results of this procedure for each of the gases and for the whole domain of E/N are presented in figure 4. The panels correspond to the swarm parameters W , D_L , ν_{eff} , and α_{eff} , respectively, and show the differences of each parameter derived by the simulation of the experimental system with respect to its theoretical value obtained from the BE solution. That is, if we denote the values obtained from the simulation of the experimental system by S , and those obtained from the BE solution by T , the quantity depicted in figure 4 is $(S - T)/T$. The set of 'Corrected' transport coefficients can thus be obtained from the experimentally measured values (X_{corr} and X_{exp} , respectively) as $X_{\text{corr}} = \frac{X_{\text{exp}}}{1 + \frac{S-T}{T}} = \frac{T}{S} X_{\text{exp}}$.

In the case of the bulk drift velocity (figure 4(a)), the error is in the few % range for most of the conditions, and it approaches $\approx 10\%$ at the highest E/N values. This indicates that the determination of the bulk drift velocity values from the experimental data is quite reliable.

The situation turns out to be much worse for the longitudinal component of the diffusion tensor (figure 4(b)). Here, the error ranges from $\approx -40\%$ to $\approx +80\%$, depending on E/N . The D_L data can be considered to be acceptably accurate at intermediate E/N values only. The much larger error of D_L with respect to that of W can be explained by the fact that the distribution of the average electron energy along the swarm is inhomogeneous. In the close vicinity of the maximum of the spatial distribution of the electron density, the variation of the average energy along the swarm is comparatively small. However, by moving away from this maximum, the spatial

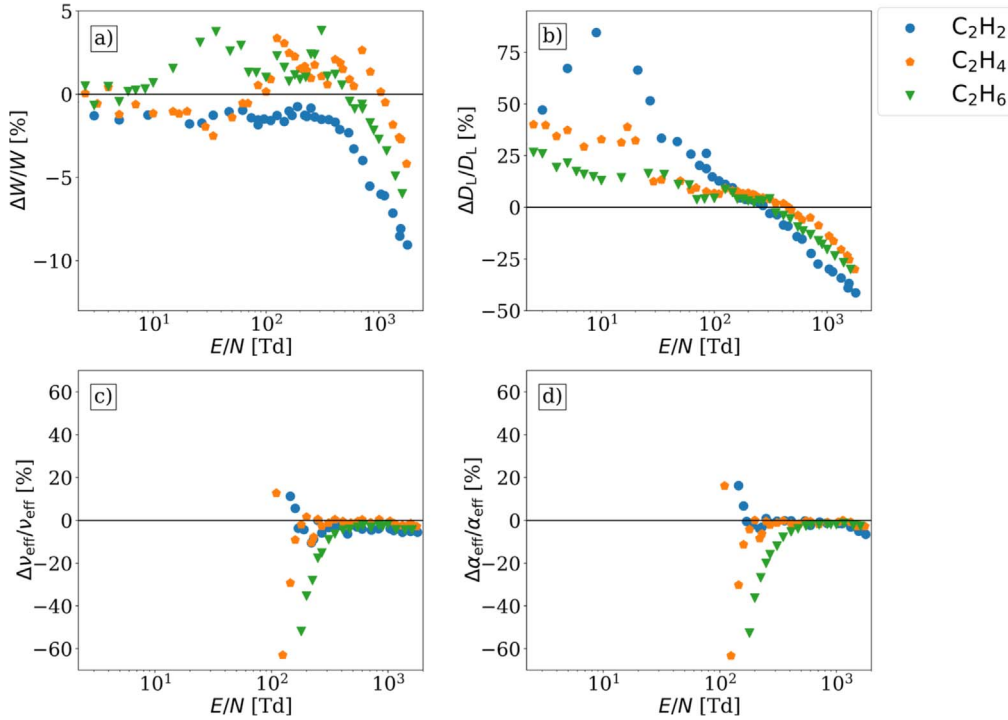


Figure 4. Deviations of the results between the swarm parameters obtained from the simulations of the experimental system (S) versus the theoretical values (T), i.e. $(S - T)/T$ for the bulk drift velocity (a), the longitudinal component of the diffusion tensor (b), the effective ionization frequency (c) and the effective SST ionization coefficient (d). Applying these correction factors to the experimental results (X_{exp}) leads to the set of ‘Corrected’ transport coefficients (X_{corr}) as $X_{\text{corr}} = \frac{X_{\text{exp}}}{1 + \frac{S-T}{T}} = \frac{T}{S} X_{\text{exp}}$.

variations of the average energy along the swarm increase. As the drift velocity is primarily determined by the position of the maximum of the spatial profile of the electron density while the diffusion is predominantly determined by the width of this distribution, it is clear that the width of the distribution is more affected by non-uniform sensitivity of the detector with respect to the average electron energy than the position of the maximum.

Regarding the effective ionization frequency (figure 4(c)) and the strongly related SST ionization coefficient (figure 4(d)), we observe small errors at high E/N values, where ionization is appreciable. The error, on the other hand, grows high when E/N approaches ≈ 100 Td, where both ν_{eff} and α_{eff} drop rapidly.

5. Results and discussion

The electron swarm parameters have been measured in a wide range of the reduced electric field, between 1 and 1790 Td at a gas temperature T of 293 K. The pressure of the gases ranged between 5 and 1000 Pa in the measurements. The actual value for any given E/N was set to optimize the measured current of the drift cell, while paying attention that the corresponding voltage remains below the breakdown threshold over the whole range of the electrode distances covered during the scanning process.

In the following, results of our measurements are presented for the three hydrocarbon gases C_2H_2 , C_2H_4 , and

C_2H_6 . Besides the transport parameters and ionization coefficients resulting from the experiments via the fitting procedure described in section 1, we also present the corrected values of these data resulting from the procedure introduced in section 4. For each swarm parameter, we compare the present measured data with previous experimental results and with the results of the kinetic computations based on the solution of the electron BE or on MC simulations, obtained with the selected electron collision cross sections. The results for the *flux* parameters obtained by methods BE 0D, BE DG and MC overlap, and so do the *bulk* parameters obtained from the BE DG and MC methods. Our experimental results for each transport parameter and gas (uncorrected and corrected values) are available in the supplementary data file (online at stacks.iop.org/PSST/29/045009/mmedia) Furthermore, the present measured data as well as results of the kinetic computations are available online at [46–48].

5.1. Electron mobility

We start by comparing the values of the gas number density times mobility, $N\mu$, derived from the bulk drift velocity, with previous experimental data for the three hydrocarbon gases in figure 5. We estimate the maximum experimental error of these values to be around 6%.

Except for the high values of E/N , our measured *bulk* drift velocity and mobility results are in excellent agreement with all previous results. In C_2H_2 , however, at low E/N we find two distinct sets of results: the present results are

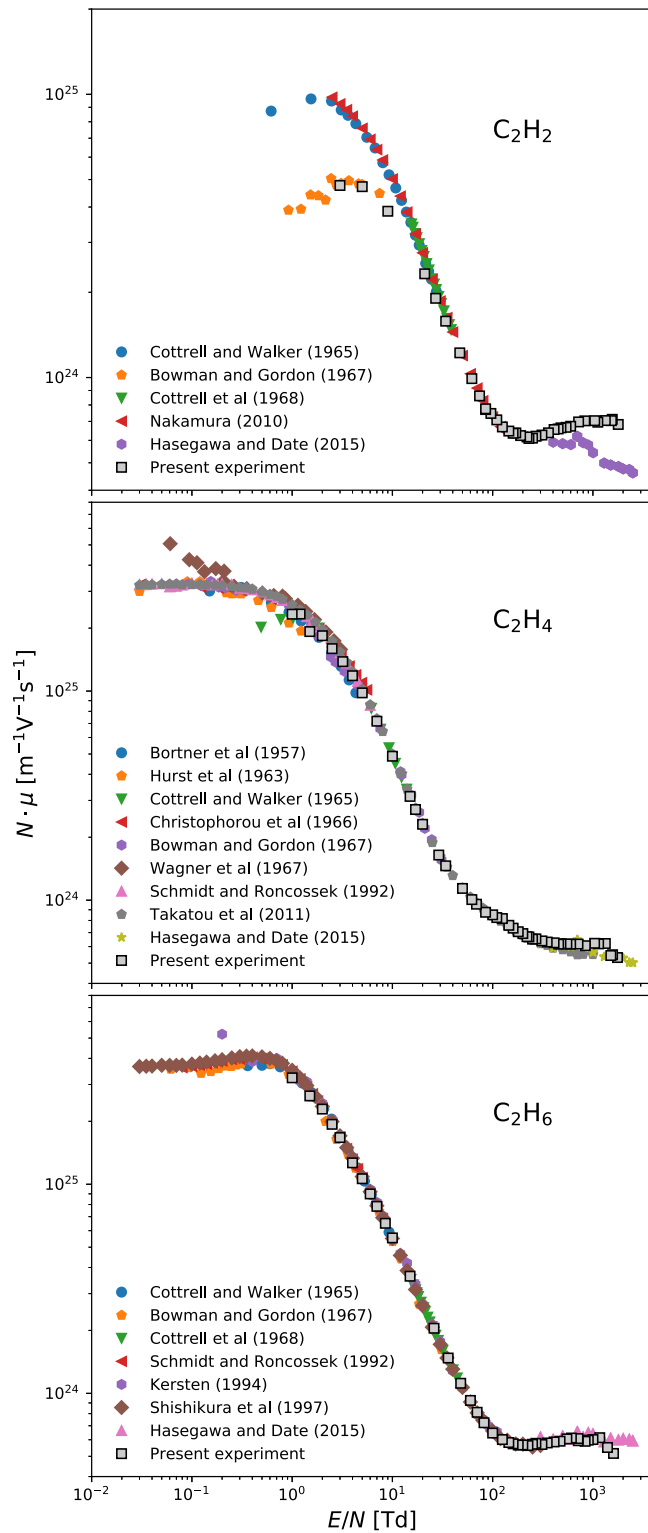


Figure 5. Mobility in C_2H_2 , C_2H_4 and C_2H_6 obtained from drift velocity results: Bortner *et al* [23], Hurst *et al* [22], Cottrell and Walker [17], Christophorou *et al* [21], Bowman and Gordon [16], Wagner *et al* [20], Cottrell *et al* [15], Schmidt and Roncossek [19], Kersten [25], Shishikura *et al* [24], Nakamura [14], Takatou *et al* [18], Hasegawa and Date [13] and present measurements. The figures share the same E/N scale. ‘Present experiment’ corresponds to the uncorrected experimental data. The corrected data are not shown here because of the small correction factors for the bulk drift velocity and the mobility.

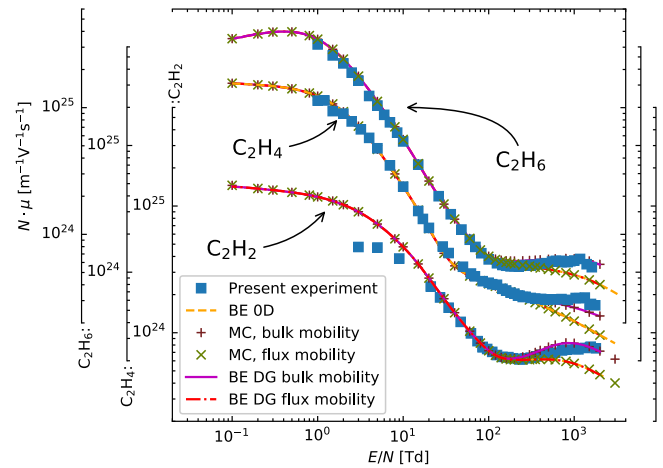


Figure 6. Mobility in C_2H_2 , C_2H_4 and C_2H_6 ; present experiment and modeling results. The results and $N\mu$ scale for C_2H_4 and C_2H_6 have been shifted. ‘Present experiment’ corresponds to the uncorrected experimental data. The corrected data are not shown here because of the small correction factors for the bulk drift velocity/mobility.

consistent with the measurements of Bowman and Gordon [16], while the results of Cottrell and Walker [17] are in accordance with those of Nakamura [14]. Note that the latter results were used to obtain the recommended electron collision cross sections for C_2H_2 [39] used in the present modeling and simulation. At high E/N the present results deviate from those of Hasegawa and Date [13] in C_2H_2 and C_2H_4 . However the latter results are obtained from the mean arrival-time velocity defined in [49] and are not easily comparable with the present TOF results in the presence of reaction processes.

In figure 6 we compare the results of the present measurements with the kinetic computation results. In this figure the E/N scale is common to the three gases but the $N\mu$ scale and data for C_2H_4 and C_2H_6 have been shifted upwards to avoid overlapping of the curves. Above 200 Td the contribution of non-conservative processes becomes visible and the mobility results are split into a *bulk* branch (for MC and BE DG *bulk* mobilities and the present measurements) and *flux* values (respectively for BE 0D, MC and BE DG *flux* mobilities). Here our measured data show some differences to the MC and BE DG *bulk* results for all three gases. In case of C_2H_2 , as the electron collision cross sections used are based on the swarm results of Nakamura [14], the modeling results deviate from the present experimental results below 10 Td. Note that below 3 Td the modeling results also deviate from the measurements of Bowman and Gordon [16] as well as of Cottrell and Walker [17] in figure 5.

5.2. Diffusion tensor

The present experimental results for the gas number density times the longitudinal component of the diffusion tensor, $N D_L$, for C_2H_2 , C_2H_4 and C_2H_6 are shown in figure 7 together with previously measured data as well as with the kinetic computation values for the *bulk* longitudinal and

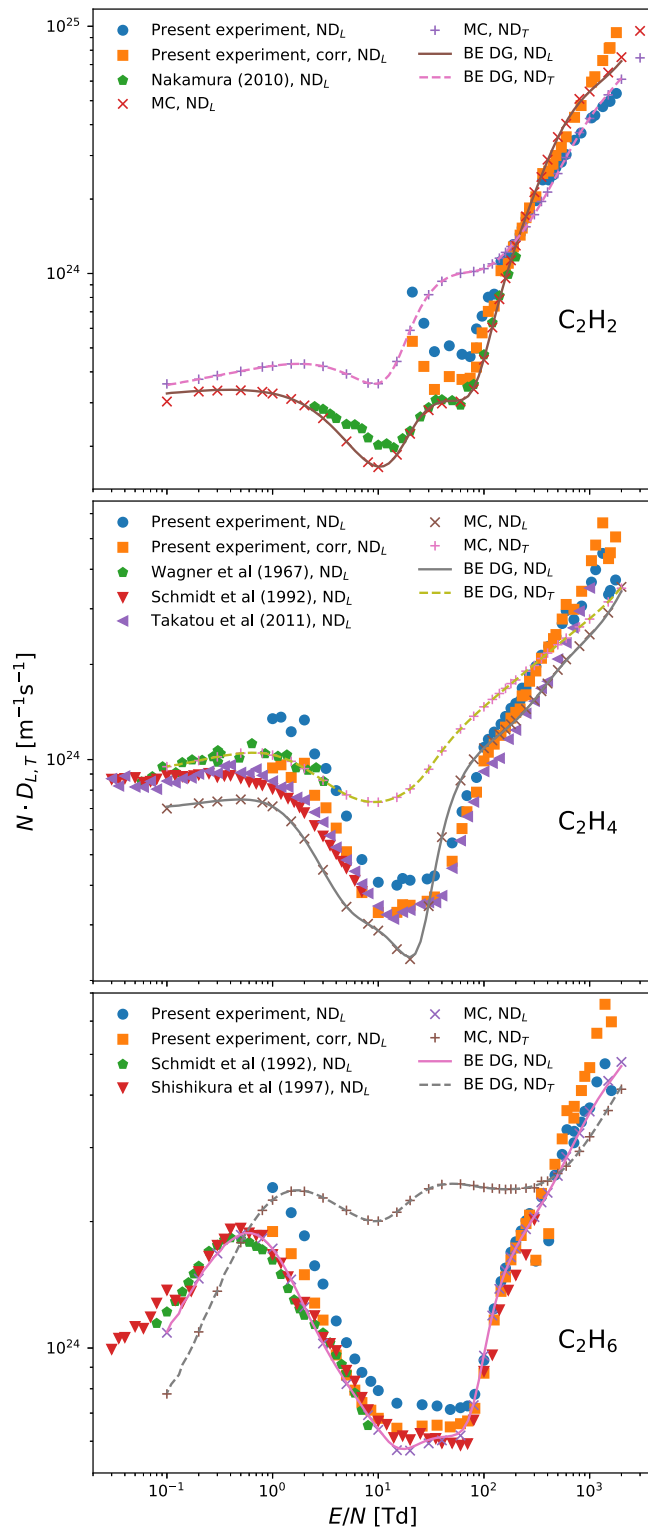


Figure 7. Longitudinal and transverse *bulk* components of the diffusion tensor in C_2H_2 , C_2H_4 and C_2H_6 . Experimental results: present experiment, Wagner *et al* [20], Schmidt and Roncossek [19], Shishikura *et al* [24], Nakamura [14], Takatou *et al* [18]. Modeling results: MC and BE DG (ND_L and ND_T). The figures share the same E/N scale. The panels show both the uncorrected and corrected experimental results of this study.

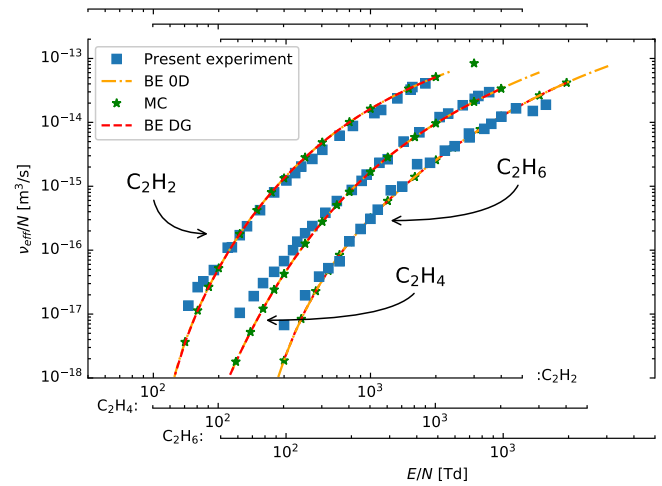


Figure 8. Reduced effective ionization frequency in C_2H_2 , C_2H_4 and C_2H_6 : present experiment and modeling results. The results and E/N scale for C_2H_4 and C_2H_6 are shifted horizontally. ‘Present experiment’ corresponds to the uncorrected data.

transverse components of the diffusion tensor for each gas. The present measured values of $N D_L$ exhibit larger scattering, which is explained by the higher uncertainty of the determination of D_L in the experiments ($\approx 10\%$) compared to that of the drift velocity.

Above 100 Td there is reasonable agreement of the present measurements with previous experimental data and the modeling results for the three gases. Below 100 Td however, the present measurements evidence the same qualitative behavior but are systematically above previous measurements. Note that the application of the correction procedure, detailed in section 4, to our experimental results leads to much better agreement with previously measured data, in particular for C_2H_4 and C_2H_6 . In case of C_2H_2 , we observe a qualitative difference between our measurements and those performed by Nakamura [14]. These differences can be attributed to the non-uniform sensitivity of the detector in our experimental setup, which has been already discussed in section 4.

The modeling results for D_L in C_2H_2 and C_2H_4 below 2 Td and 5 Td, respectively, also deviate from all experimental results indicating that the corresponding cross section sets require improvement. In each of the three gases, the values of the transverse component of the diffusion tensor, D_T , obtained by the kinetic computations, are very different from the longitudinal component, D_L . The measurement of data of this component can provide additional tests for the fitting of the electron collision cross sections.

5.3. Effective ionization frequency and SST ionization coefficient

The experimental and modeling results for the reduced effective ionization frequency, ν_{eff}/N , for the three gases

studied are displayed in figure 8. To our best knowledge this is the first report of ν_{eff} in these three gases for an extended range of $100 \text{ Td} \leq E/N \leq 1790 \text{ Td}$, for which the estimated experimental error of the data is $\leq 8\%$. In order to accommodate the results on the same figure, all gases share the same ν_{eff}/N axis but the E/N scales for C_2H_4 and C_2H_6 have been shifted to the right.

Good agreement between our measured and calculated results is generally found for E/N values larger than about 200 Td, indicating that the electron collision cross section sets for the three gases are reasonably well adapted to allow for an appropriate determination of the rate coefficients for ground state ionization. Certain differences are obvious for lower E/N values. These differences seem to result from the measurement and/or, more likely, from the fitting procedure (see figure 4).

Our experimental data for the reduced effective SST ionization coefficient, α_{eff}/N , obtained using equation (2), are compared with previous measurements and the kinetic computation results in figure 9. As α_{eff} is derived from the set of parameters $\{W, D_L, \nu_{\text{eff}}\}$, these results have a higher uncertainty than ν_{eff} with an estimated experimental error of $\leq 10\%$. Notice that the kinetic computation results using method BE SST do not include the approximations involved in equation (2), but are directly obtained by solving the electron BE at SST conditions according to (7). In this respect, their comparison with the BE DG and MC results can indicate the range of validity of equation (2).

Except for the low values of E/N , our results for the effective SST ionization coefficient are in excellent agreement with all previous results and the kinetic computations. At values close to the threshold, however, the present results are higher than previous measurements. Notice that Kersten's effective Townsend ionization coefficient was measured under TOF conditions and corresponds to ν_{eff}/W [25]. Thus, it represents the effective SST ionization coefficient α_{eff} according to (2) only in the absence of diffusion, i.e. $D_L = 0$.

5.4. Effect of the vibrationally excited population

The cross sections sets used above were obtained considering only electron collisions with the ground state of the molecules. However, the correct description of the characteristics of electrons in molecular gases at low reduced electric fields, requires to take into account superelastic collisions of electrons with thermally excited molecules. For example, this is discussed in [50] for the case of molecular hydrogen and nitrogen. For diatomic molecules superelastic collisions with rotationally excited molecules have to be taken into account in calculations for low reduced electric fields (see, for example [51]).

As polyatomic molecules have multiple vibrational modes and these modes can be degenerate, in these gases we can find a significant fraction of molecules in thermally excited vibrational states at room temperature. In addition to their contribution to energy losses due to elastic, exciting, ionizing and attaching collision processes, these excited states contribute to electron energy gains due to superelastic

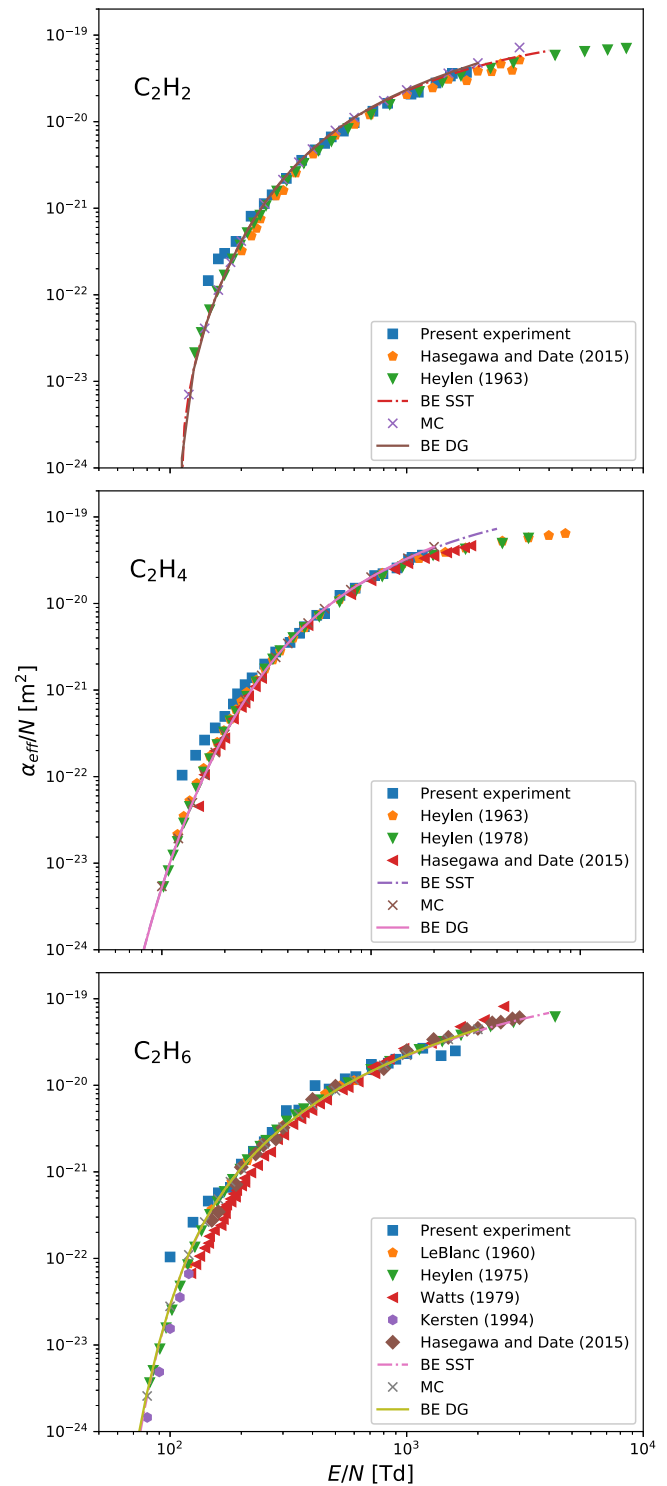


Figure 9. Reduced effective Townsend ionization coefficient in C_2H_2 , C_2H_4 and C_2H_6 . Experimental results: present experiment, Heylen [26, 29], Watts and Heylen [28], Kersten [25] and Hasegawa and Date [13]. Modeling results: BE SST, MC and BE DG. ‘Present experiment’ corresponds to the uncorrected data.

collisions and influence the EVDF and transport parameters, mainly at low to medium E/N field values. The importance of their effect increases with the energy associated with the collision and the fractional population of thermally excited states with that energy. This population, however, decreases

Table 1. Fractional population of the first vibrational levels of C₂H₂ at 293.15 K.

Vibr. state	Short notation	g	Energy (eV)	Frac pop. (%)
(00000)	ν_0	1	0.0	85.37
(10000)	ν_1	1	0.421	5.5×10^{-6}
(01000)	ν_2	1	0.245	5.3×10^{-3}
(00100)	ν_3	1	0.411	8.3×10^{-6}
(00010)	ν_4	2	0.075	8.47
(00020)		3	0.150	0.63
(00001)	ν_5	2	0.0905	4.75
(00002)		3	0.180	0.20
(00011)	$\nu_4 + \nu_5$	4	0.165	0.47

exponentially with energy. From the combination of these two factors, the effect on the EVDF should be maximum for a given energy value.

Taking into account the equations for the fractional populations and statistical weights of polyatomic molecules in the [appendix](#), we can estimate the populations of the different states of these gases.

Acetylene has five vibrational modes, with the two bending modes (ν_4 and ν_5) double degenerate and with energies of, respectively, 0.075 eV and 0.0905 eV [52]. At a gas temperature of 293.15 K, the vibrational states with fractional population above 0.1% are indicated in table 1. At this temperature only around 85% of the acetylene molecules are in the ground state and the vibrational population in excited states of modes ν_4 and ν_5 is significant.

Ethylene: In contrast to C₂H₂, none of the twelve ethylene vibrational modes [52] is degenerate, where the lowest threshold energy for vibrational excitation to ν_{10} is 0.102 eV and, at the same temperature, more than 95% of the molecules are in the ground state.

Ethane: All the degenerate vibrational modes of ethane [52] have energies above 0.15 eV and at room temperature their fractional population is small. Overall, however, only 73% of ethane molecules are in the ground state as mode ν_4 has an excitation energy of only 0.036 eV. Molecules in the two first excited vibrational states of this mode represent 22% of the total. On the other hand, as the excitation energy of the ν_4 mode transitions is very small, the effect on the EVDF and transport parameters is also small.

Of the three gases analyzed, the impact of the thermally excited vibrational population on the EVDF should be largest in C₂H₂. The vibrational excitation cross section set for C₂H₂ [39] is also more complete than the vibrational cross section sets for C₂H₄ and C₂H₆ used in this study. For these reasons we study the effect of the thermally excited vibrational states only for acetylene.

Our goal is to single out the contribution of the vibrationally excited molecules due to superelastic collisions and we will change the electron collision cross sections in such a way that, if we neglect these collisions, we obtain the same

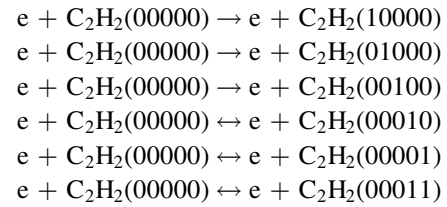
results as before. Starting from the recommended cross section set for ethylene [39], we introduce the following modifications:

(a) We split the lumped cross sections for the vibrational excitation of modes ν_1/ν_3 and ν_4/ν_5 into individual cross sections for each modes, with a value of half of the original cross section. That is $\sigma_{\nu_1} = \sigma_{\nu_3} = \frac{1}{2}\sigma_{\nu_1/\nu_3}$ and $\sigma_{\nu_4} = \sigma_{\nu_5} = \frac{1}{2}\sigma_{\nu_4/\nu_5}$.

(b) The threshold for the excitation of modes ν_1 and ν_3 and of modes ν_4 and ν_5 is set at the same value as before of, respectively, 0.411 eV and 0.0905 eV.

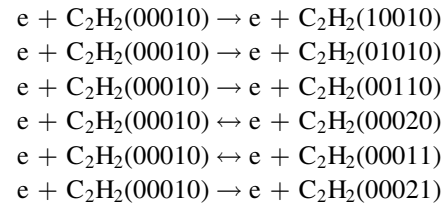
(c) We assume that all molecules are in one of the three states (00000), (00010) and (00001), with the fractional population, δ , of the last two states in thermal equilibrium with the gas and the ground state fraction given by $\delta_{00000} = (1 - \delta_{00010} - \delta_{00001})$.

(d) We consider the following vibrational excitation processes for electron collisions with the ground state (00000):

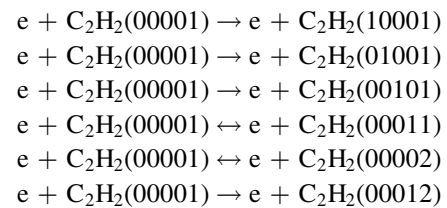


where reactions with double-arrows include superelastic collisions.

(e) We additionally include the following vibrational excitation processes on collisions with states (00010) and (00001):



and



adopting for these processes the same cross sections as the corresponding excitations from the ground state.

(f) We further assume that the electron collision cross sections for momentum transfer, electronic excitation, ionization and attachment with the vibrational states (00010) and (00001) are the same as for state (00000).

(g) We obtain the superelastic vibrational cross sections from the corresponding direct processes assuming that the detailed balance principle is valid.

Note that if we neglect superelastic collisions, the EVDF and swarm parameters obtained with these modified cross sections and electron collision reactions are exactly the same

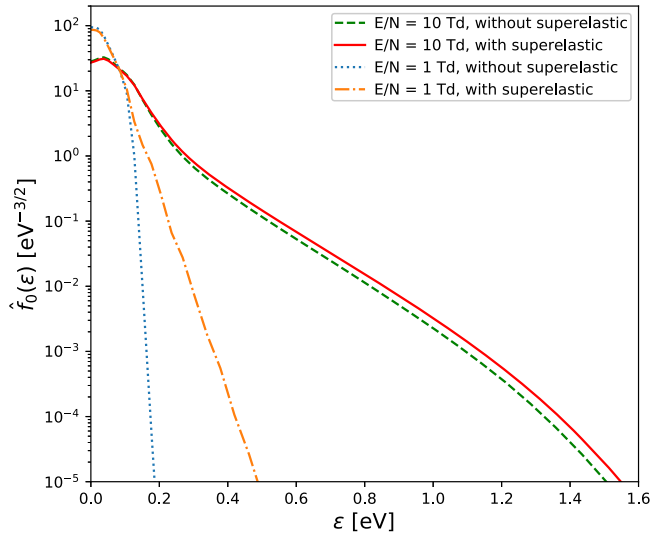


Figure 10. Isotropic component of the EVDF in C_2H_2 at 293.15 K for 1 and 10 Td, with and without superelastic collision processes included.

as with the original set [39] and are independent of the fractional population of levels (00010) and (00001).

The influence of superelastic collisions is illustrated in figure 10 which shows the isotropic component $\hat{f}_0(\epsilon)$ of the EVDF as a function of the electron kinetic energy, $\epsilon = m_e v^2/2$, calculated at E/N values of 1 Td and 10 Td, respectively, with and without the inclusion of superelastic processes. Pronounced differences between the corresponding isotropic distributions $\hat{f}_0(\epsilon)$ are found at $E/N = 1$ Td, while the impact of superelastic electron collision processes is comparatively small at 10 Td. This finding is not only reflected by the isotropic distribution but also by different macroscopic properties.

The influence of superelastic collisions is mostly visible in the drift velocity and mobility as shown in figure 11. This figure compares the values of mobility and the longitudinal and transverse *bulk* components of the diffusion tensor obtained with the original cross sections set with the results obtained using the modified set with and without the inclusion of superelastic processes. As predicted, the results of the modified set neglecting superelastic collisions are the same as those obtained with the original set. Superelastic collisions are responsible for a reduction of the electron mobility in the range of low reduced field, visible up to approximately 20 Td. The influence on the components of the diffusion tensor is overall smaller than that on the mobility with the largest differences in the longitudinal component around 10 Td.

As the impact of superelastic collisions decreases remarkably above about 20 Td, their influence on the effective ionization frequency and Townsend ionization coefficient is negligible.

6. Concluding remarks

We have investigated electron swarm parameters in C_2H_2 , C_2H_4 and C_2H_6 experimentally using a scanning drift tube, as

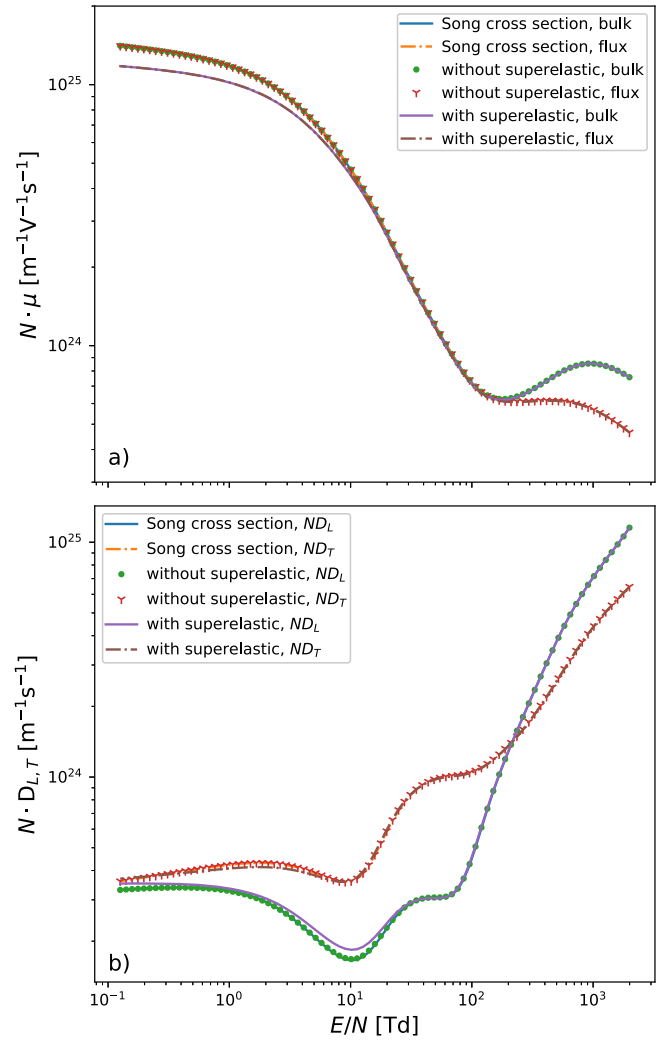


Figure 11. (a) Mobility and (b) longitudinal and transverse *bulk* components of the diffusion tensor in C_2H_2 at 293.15 K: modeling results obtained with the electron collision cross sections from [39] without considering superelastic processes and with a modified set with and without superelastic processes.

well as computationally by solutions of the electron BE and via MC simulation, corresponding to both TOF and SST conditions. The measured data made it possible to derive the bulk drift velocity, the bulk longitudinal component of the diffusion tensor and the effective ionization frequency of the electrons, for the wide range of the reduced electric field from 1 to 1790 Td. The measured TOF transport parameters as well as the effective SST ionization coefficient, deduced from the TOF swarm parameters, have been compared to experimental data obtained in previous studies. Here, generally good agreement with most of the transport parameters and the effective SST ionization coefficients obtained in these earlier studies was found. In the case of the drift velocity or the mobility, respectively, and the longitudinal component of the diffusion tensor we found disagreements at low or high values of E/N .

The experimental data have undergone a correction procedure, which was supposed to quantify the errors caused by the dependence of the sensitivity of the detector of the drift

cell on the energy distribution of the electrons in the swarm that may have a spatial dependence.

In particular, in case of C_2H_2 our measured drift velocities at low E/N agree well with previous data of Bowman and Gordon [16] but not with the results of Cottrell and Walker [17] as well as of Nakamura [14]. Further measurements in this range are required to clarify this contradiction.

The comparison of the experimental data was also carried out with swarm parameters resulting from various kinetic computations, which used the most recently recommended cross section sets [24, 39, 40]. Here, excellent agreement between electron BE and MC simulation results verifies the computational approaches and data for the three gases. The agreement of the computed data with the present and previously measured values of the reduced effective ionization frequency and SST ionization coefficient was generally good. However, certain differences between kinetic computational and measured results found for the drift velocities and, especially, for the longitudinal component of the diffusion tensor illustrate the need for an improvement of the existing collision cross section sets for the three hydrocarbon gases considered.

We have also studied the influence of the thermally excited vibrational populations on the transport parameters. In the case of C_2H_2 we have found that this population has a significant value and superelastic collisions influence the drift velocity and the components of the diffusion tensor up to 20 Td. The fitting of electron collision cross sections for this gas using swarm experiments should include these processes.

Acknowledgments

This work was partially supported by the Portuguese FCT–Fundação para a Ciência e a Tecnologia, under project UID/FIS/50010/2013, by the Hungarian Office for Research, Development and Innovation (NKFIH) grants K119357, K115805, by the ÚNKP-19-3 New National Excellence Program of the Ministry for Innovation and Technology, and funded by the Deutsche Forschungsgemeinschaft (DFG, German Research Foundation)—project number 327886311. SD and DB are supported by Grants No. OI171037 and III41011 from the Ministry of Education, Science and Technological Development of the Republic of Serbia. We thank Professor Y Nakamura for providing numerical values of measured electron transport parameters in C_2H_2 and Mr T Szűcs for his contributions to the construction of the experimental apparatus.

Appendix. Statistical weights and statistical sums

The fractional populations for the levels of a polyatomic molecule with n_v modes and vibrational quantum numbers $(v_1v_2v_3\dots)$ are given by

$$\delta_{(v_1v_2v_3\dots)} = \frac{g_{(v_1v_2v_3\dots)}}{Q_v} \exp\left(-\frac{\epsilon_{(v_1v_2v_3\dots)}}{k_B T}\right), \quad (\text{A.1})$$

where $\epsilon_{(v_1v_2v_3\dots)}$ is the level energy and g the total statistical weight


$$g_{(v_1v_2v_3\dots)} = \prod_{n=1}^{n=n_v} \frac{(v_n + d_n - 1)!}{v_n!(d_n - 1)!}, \quad (\text{A.2})$$

where d_n is the degeneracy multiplicity for mode n , and Q_v the vibrational statistical sum which, in the harmonic oscillator approximation for the vibrational states, is

$$Q_v = \prod_{n=1}^{n=n_v} (1 - Z_n)^{-d_n}, \quad Z_n = \exp\{-h\nu_n/k_B T\}, \quad (\text{A.3})$$

where h is the Planck constant and ν_n are the vibrational frequencies.

ORCID iDs

N R Pinhão  <https://orcid.org/0000-0002-4185-2619>
 D Loffhagen  <https://orcid.org/0000-0002-3798-0773>
 M Vass  <https://orcid.org/0000-0001-9865-4982>
 P Hartmann  <https://orcid.org/0000-0003-3572-1310>
 I Korolov  <https://orcid.org/0000-0003-2384-1243>
 S Dujko  <https://orcid.org/0000-0002-4544-9106>
 D Bošnjaković  <https://orcid.org/0000-0002-2725-5287>
 Z Donkó  <https://orcid.org/0000-0003-1369-6150>

References

- [1] Adamovich I V and Lempert W R 2014 *Plasma Phys. Control. Fusion* **57** 014001
- [2] Starikovskiy A and Aleksandrov N 2013 *Prog. Energy Combust. Sci.* **39** 61–110
- [3] Kosarev I, Aleksandrov N, Kindysheva S, Starikovskaia L S and Starikovskii A Y 2009 *Combust. Flame* **156** 221–33
- [4] Kosarev I, Pakhomov A, Kindysheva S, Anokhin E and Aleksandrov N 2013 *Plasma Sources Sci. Technol.* **22** 045018
- [5] Kosarev I, Kindysheva S, Aleksandrov N and Starikovskiy A Y 2015 *Combust. Flame* **162** 50–9
- [6] Kosarev I, Kindysheva S, Momot R, Plastinin E, Aleksandrov N and Starikovskiy A Y 2016 *Combust. Flame* **165** 259–71
- [7] Robertson J 2002 *Mater. Sci. Eng. R* **37** 129–281
- [8] Kumar M and Ando Y 2010 *J. Nanosci. Nanotechnol.* **10** 3739–58
- [9] Fonte P and Peskov V 2010 *Plasma Sources Sci. Technol.* **19** 034021
- [10] von Keudell A, Schwarz-Selinger T, Jacob W and Stevens A 2001 *14th Int. Conf. on Plasma-Surface Interactions in Controlled Fusion Devices; J. Nucl. Mater.* **290-293** 231–7
- [11] Varanasi P, Giver L and Valero F 1983 *J. Quant. Spectrosc. Radiat. Transfer* **30** 497–504
- [12] Courtin R, Gautier D, Marten A, Bezard B and Hanel R 1984 *Astrophys. J.* **287** 899–916
- [13] Hasegawa H and Date H 2015 *J. Appl. Phys.* **117** 133302
- [14] Nakamura Y 2010 *J. Phys. D: Appl. Phys.* **43** 365201
- [15] Cottrell T L, Pollock W J and Walker I C 1968 *Trans. Faraday Soc.* **64** 2260–6
- [16] Bowman C R and Gordon D E 1967 *J. Chem. Phys.* **46** 1878–83

- [17] Cottrell T L and Walker I C 1965 *Trans. Faraday Soc.* **61** 1585–93
- [18] Takatou J, Sato H and Nakamura Y 2011 *J. Phys. D: Appl. Phys.* **44** 315201
- [19] Schmidt B and Roncossek M 1992 *Aust. J. Phys.* **45** 351–64
- [20] Wagner E B, Davis F J and Hurst G S 1967 *J. Chem. Phys.* **47** 3138–47
- [21] Christophorou L G, Hurst G S and Hadjiantoniou A 1966 *J. Chem. Phys.* **44** 3506–13
- [22] Hurst G S, O’Kelly L B, Wagner E B and Stockdale J A 1963 *J. Chem. Phys.* **39** 1341–5
- [23] Bortner T E, Hurst G S and Stone W G 1957 *Rev. Sci. Instrum.* **28** 103–8
- [24] Shishikura Y, Asano K and Nakamura Y 1997 *J. Phys. D: Appl. Phys.* **30** 1610–5
- [25] Kersten H J 1994 *Messung der Driftgeschwindigkeit Und Des Effektiven Townsendkoeffizienten Von Elektronen Bei Hohen Elektrischen Feldstärken* (Heidelberg: Diploma thesis Ruprecht-Karls-Universität) (<https://www.lxcat.net/Heidelberg>)
- [26] Heylen A E D 1963 *J. Chem. Phys.* **38** 765–71
- [27] Heylen A E D 1978 *Int. J. Electron.* **44** 367–74
- [28] Watts M P and Heylen A E D 1979 *J. Phys. D: Appl. Phys.* **12** 695–702
- [29] Heylen A E D 1975 *Int. J. Electron.* **39** 653–60
- [30] LeBlanc O H and Devins J C 1960 *Nature* **188** 219–20
- [31] Blevin H A and Fletcher J 1984 *Aust. J. Phys.* **37** 593–600
- [32] Donkó Z, Hartmann P, Korolov I, Jeges V, Bošnjaković D and Dujko S 2019 *Plasma Sources Sci. Technol.* **28** 095007
- [33] Ramo S 1939 *Proc. IRE* **27** 584
- [34] Korolov I, Vass M, Bastykova N K and Donkó Z 2016 *Rev. Sci. Instrum.* **87** 063102
- [35] Korolov I, Vass M and Donkó Z 2016 *J. Phys. D: Appl. Phys.* **49** 415203
- [36] Vass M, Korolov I, Loffhagen D, Pinhão N and Donkó Z 2017 *Plasma Sources Sci. Technol.* **26** 065007
- [37] Shockley W 1938 *J. Appl. Phys.* **9** 635
- [38] Sirkis M and Holonyak N 1966 *Am. J. Phys.* **34** 943
- [39] Song M Y, Yoon J S, Cho H, Karwasz G P, Kokoouline V, Nakamura Y and Tennyson J 2017 *J. Phys. Chem. Ref. Data* **46** 013106
- [40] Fresnet F, Pasquiers S, Postel C and Puech V 2002 *J. Phys. D: Appl. Phys.* **35** 882–90
- [41] Leyh H, Loffhagen D and Winkler R 1998 *Comput. Phys. Commun.* **113** 33–48
- [42] Kumar K, Skullerud H and Robson R 1980 *Aust. J. Phys.* **33** 343–448
- [43] Segur P, Bordage M C, Balaguer J P and Youssi M 1983 *J. Comput. Phys.* **50** 116–37
- [44] Dujko S, White R D, Petrović Z L and Robson R E 2010 *Phys. Rev. E* **81** 046403
- [45] Dujko S, White R D, Petrović Z L and Robson R E 2011 *Plasma Sources Sci. Technol.* **20** 024013
- [46] Loffhagen D, Pinhão N R, Vass M, Hartmann P, Korolov I, Dujko S, Bošnjaković D and Donkó Z 2020 Electron Swarm Parameters in C₂H₂—Measurements and Kinetic Calculations (<https://doi.org/10.34711/inptdat.112>)
- [47] Loffhagen D, Pinhão N R, Vass M, Hartmann P, Korolov I, Dujko S, Bošnjaković D and Donkó Z 2020 Electron Swarm Parameters in C₂H₄—Measurements and Kinetic Calculations (<https://doi.org/10.34711/inptdat.122>)
- [48] Loffhagen D, Pinhão N R, Vass M, Hartmann P, Korolov I, Dujko S, Bošnjaković D and Donkó Z 2020 Electron Swarm Parameters in C₂H₆—Measurements and Kinetic Calculations (<https://doi.org/10.34711/inptdat.124>)
- [49] Kondo K and Tagashira H 1990 *J. Phys. D: Appl. Phys.* **23** 1175–83
- [50] Frost L S and Phelps A V 1962 *Phys. Rev.* **127** 1621–33
- [51] Ridenti M A, Alves L L, Guerra V and Amorim J 2015 *Plasma Sources Sci. Technol.* **24** 035002
- [52] Shimanouchi T 1972 *Tables of Molecular Vibrational Frequencies Consolidated Volume I Report* NSRDS-NBS 39 National Bureau of Standards, Washington